

Lawrence Berkeley National Laboratory

LBL Publications

Title

Experimental evidence of reaction-induced fracturing during olivine carbonation

Permalink

<https://escholarship.org/uc/item/0k01f3w2>

Journal

Geophysical Research Letters, 43(18)

ISSN

0094-8276

Authors

Zhu, Wenlu
Fusseis, Florian
Lisabeth, Harrison
[et al.](#)

Publication Date

2016-09-28

DOI

10.1002/2016gl070834

Peer reviewed

Experimental evidence for chemo-mechanical coupling during carbon mineralization in ultramafic rocks

Author links open overlay panel [H.P.Lisabeth^{ab}](#) [W.Zhu^a](#) [P.B.Kelemen^c](#) [A.Ilgen^d](#)
Show more

<https://doi.org/10.1016/j.epsl.2017.06.045> [Get rights and content](#)

Highlights

- Deformation experiments run on carbonic acid-saturated dunites.
 - Magnesite and serpentine precipitated in pore space.
 - Reaction reduces strength, Young's modulus and permeability.
 - Olivine dissolution rate increased by mechanical stress.

Abstract

Storing [carbon dioxide](#) in the subsurface as carbonate minerals has the benefit of long-term stability and immobility. [Ultramafic rock](#) formations have been suggested as a potential reservoir for this type of storage due to the availability of [cations](#) to react with dissolved carbon dioxide and the fast reaction rates associated with minerals common in ultramafic formations; however, the rapid reactions have the potential to couple with the mechanical and hydraulic behavior of the rocks and little is known about the extent and mechanisms of this coupling. In this study, we argue that the dissolution of primary minerals and the precipitation of [secondary minerals](#) along pre-existing fractures in samples lead to reductions in both the apparent [Young's modulus](#) and [shear strength](#) of aggregates, accompanied by reduction in permeability. [Hydrostatic](#) and triaxial deformation experiments were run on [dunite](#) samples saturated with de-ionized water and carbon dioxide-rich solutions while stress, [strain](#), permeability and [pore](#) fluid chemistry were monitored. Sample [microstructures](#) were examined after reaction and deformation using [scanning electron microscopy](#) (SEM). The results show that channelized dissolution and carbonate mineral precipitation in the samples saturated

with carbon dioxide-rich solutions modify the structure of [grain boundaries](#), leading to the observed reductions in [stiffness](#), strength and permeability. A geochemical model was run to help interpret fluid chemical data, and we find that the apparent reaction rates in our experiments are faster than rates calculated from powder reactors, suggesting mechanically enhanced reaction rates. In conclusion, we find that chemo-mechanical coupling during [carbon mineralization](#) in dunites leads to substantial modification of mechanical and hydraulic behavior that needs to be accounted for in future modeling efforts of in situ carbon mineralization projects.

Graphical abstract

1. [Download high-res image \(120KB\)](#)
 2. [Download full-size image](#)
- [Previous article in issue](#)
 - [Next article in issue](#)

Keywords

rock deformation

permeability

carbon sequestration, storage and utilization (CSSU)

ultramafic

chemo-mechanical coupling

fluid-rock interaction

1. Introduction

As levels of atmospheric [carbon dioxide](#) continue to rise, scientists and engineers search for strategies to mitigate climatic impacts. Carbon capture, storage and utilization (CCSU) has been suggested as a key technology for controlling the near-term [carbon budget](#) (IPCC, 2014). Due to its long-term stability, [carbon mineralization](#), or the trapping of carbon dioxide in carbonate minerals, has garnered significant attention (Seifritz, 1990, Lackner et al., 1995). Initial successes at the Carbfix project in Iceland indicate that CO₂ can be rapidly mineralized in a reactive mafic reservoir (Matter et al., 2016), but many questions about the long-term behavior of such projects remain. Increased awareness of [climate change](#) and proposed geoengineering solutions have motivated a number of studies of the carbon dioxide – water – [olivine](#) system in the past decades, mostly focused on chemical and mineralogical evolution. Olivine is a commonly occurring mineral, found in many [basalts](#) and in great abundance in [ultramafic rocks](#). The dissolution of olivine has one of the fastest rates among Mg-bearing minerals and the magnesium carbonate minerals produced are thermodynamically stable and relatively insoluble in groundwater (Guyot et al., 2011). The olivine carbonation reaction is exothermic, so along with engineered injection tactics, an in-situ reservoir could be maintained at optimal reaction temperature without additional input of energy (Kelemen and Matter, 2008). Alternatively, engineered systems emulating natural processes could capture CO₂ from thermally convecting seawater passing through olivine-rich rocks, and return of carbon depleted water to the surface could draw down atmospheric CO₂ providing a relatively inexpensive method of “air capture” (Kelemen and Matter, 2008, Kelemen et al., 2011). The conversion of olivine to [magnesite](#) and [quartz](#) has a positive change in volume, which has been invoked as both a potential [porosity](#) reducing (Xu et al., 2013, Hövelmann et al., 2012) and porosity generating mechanism (Kelemen and Matter, 2008, Kelemen and Hirth, 2012).

There have been a number of studies of powdered olivine in batch reactors seeking to constrain carbonation rates (Chen et al., 2006, King et al., 2010, Daval et al., 2011, Olsson et al., 2012, Gadikota et al., 2014, Johnson et al., 2014), but experiments in aggregates suggest that reaction rates are controlled by grain-scale structure rather than kinetics (van Noort et al., 2013). Flow-through experiments tend to yield dissolution-dominated behavior, with increases in [pore space](#) and permeability near injection sites and [secondary mineral](#) precipitation at sites of low hydraulic throughput (Andreani et al., 2009, Peuble et al., 2015a). In other experiments, precipitation dominates, yielding reductions in porosity and permeability (Hövelmann et al., 2012, Godard et al., 2013). Recently, experiments have shown that extensional cracks

can be formed under confinement by non-uniform volumetric expansion due to precipitation in [porous materials](#) ([Zhu et al., 2016](#)). It remains unclear under precisely what conditions dissolution and precipitation organize to maintain permeability and facilitate complete carbonation of olivine, but the behavior appears to be related to both [thermodynamic](#) factors such as pressure, temperature and reactant [fugacities](#) and petrophysical factors such as pore size distribution and microhydrodynamics. One of the least well-understood aspects of geological [carbon sequestration](#) is the mechanical response of [reservoir rocks](#) to injection of carbon dioxide. The olivine dissolution process is sensitive to flow rate, pore geometry and crystallographic orientation ([Peuble et al., 2015b](#)), suggesting that deformation may couple with this process. Most of the research on geomechanical effects of carbon dioxide injection has focused on injection into saline [aquifers](#) (e.g. [Hawkes et al., 2005](#), [Lucier and Zoback, 2008](#), [Rutqvist, 2012](#)), and neglects chemo-mechanical feedbacks that may be relevant in more reactive reservoirs such as mafic- or ultramafic-hosted reservoirs. Tests monitoring the evolution of pore geometry and of fractures in [carbonate rocks](#) saturated with carbon dioxide rich solutions flowing through them indicate substantial changes that have hydraulic and mechanical consequences ([Elkhoury et al., 2013](#)). The [chemical alteration](#) of wellbore cement by carbon dioxide has been investigated with the motivation of better understanding borehole stability ([Kutchko et al., 2007](#), [Mason et al., 2013](#), [Huerta et al., 2012](#)) and seal integrity ([Wolterbeek et al., 2016](#)), but there is a dearth of data regarding the chemo-mechanical response of ultramafic reservoir rocks themselves to carbon dioxide injection.

How does the carbonation reaction affect the [shear strength](#) and deformation behaviors of the [host rock](#)? If there are significant effects, what are the key micromechanisms responsible? Does stress-induced [cracking](#) and dilatancy alter the permeability and thus affect carbonation rates? To answer these questions, we conducted a series of [hydrostatic](#) and triaxial deformation experiments on [dunite](#) samples undergoing carbonation reactions. These experiments were conducted at two temperatures and 3 different pore fluids were used to elucidate the coupling between mechanical and chemical load. We measured stress, [strain](#), permeability and fluid chemistry during the carbonation reaction.

2. Materials and methods

Two suites of experiments were designed to test the mechanical response of [ultramafic rocks](#) to carbonation reactions, (1) long duration (~168 h) [hydrostatic](#) pressing tests with continuous permeability, [strain](#) and fluid chemistry measurement, and (2) triaxial

deformation tests, in which shorter hydrostatic pressing (~72 h) is followed by triaxial loading. The first set of tests was conducted on samples saturated with either de-ionized water or CO₂-rich 0.6 M NaHCO₃ solution. For the second set of tests, CO₂-rich 1.5 M NaHCO₃ solution was also used as [pore](#) fluid in addition to the aforementioned two, to test the effect of [bicarbonate](#) concentration in the pore fluid. The addition of NaHCO₃ is both to buffer the pH of the pore fluid, to avoid undue stress on instrumentation, and also to provide an optimal rate of reaction ([O'Connor et al., 2002](#)).

2.1. Sample material

Experiments were run on thermally cracked Twin Sisters [dunite](#), a uniform and nearly monomineralic pristine [olivine](#) rock from the Cascade Range near Bellingham, Washington, USA. Grains were equant and range from 0.2 to 2 mm in size.

The [mineralogy](#) of the block from which samples were cored is approximately 99% olivine with trace [chromite](#), [enstatite](#) and chromium [diopside](#). The composition of the olivine is Fo₉₀ ([Ragan, 1963](#)).

Right cylinders 18.4 mm in diameter and 38.1 mm long were cored and ground out of dunite slabs. The initial permeability of the material was too low to be measured on a bench-top system (<10–18m²), and was not suitable for flow-through experiments, so samples were thermally cracked to induce sufficient permeability. Thermal [cracking](#) was accomplished by heating samples to 1250 °C in a gas-mixing furnace with a 3:1 CO–CO₂ atmosphere to prevent oxidation, then rapidly cooled. Samples were ramped to temperature in 4 h, held at temperature for 2 h, and then cooled in 6 h. Cracks result from stresses induced by anisotropic [thermal expansion](#) in olivine grains ([Demartin et al., 2004](#)). After [thermal treatment](#) samples had an average permeability of 10–15m² and average porosity of 1%. Thermal cracks were largely along [grain boundaries](#) and had high aspect ratios. The large increase in permeability attests to the interconnectivity of the new [pore space](#).

2.2. Pore fluid preparation

Three compositions of pore fluid were used for experiments, de-ionized water, CO₂-rich 0.6 M NaHCO₃ solution and CO₂-rich 1.5 M NaHCO₃ solution. The CO₂-rich solutions were prepared by mixing the desired amount of NaHCO₃ with de-ionized water, then pressurizing an external fluid-mixing vessel with 3.6 MPa of CO₂ (see Supplementary Figure S1). The fluid is allowed to equilibrate for at least 48 h before the sample is flushed. Using the online tool GEOPIG ([Johnson et al., 1992](#)) to calculate equilibrium constants for CO₂ dissolution reactions at experimental conditions, we calculate

the $p\text{CO}_2$ at experimental conditions to be 0.8 MPa. The fluid-mixing vessel is plumbed into the [pore pressure](#) system of the triaxial deformation apparatus, and the pressure controlled by upstream and downstream intensifiers in order to move the fluid through the system without depressurizing and degassing CO_2 . According to the [equation of state](#) of Duan and Sun (2003), the amount of dissolved CO_2 in the system remains below the solvus for the duration of the experimental procedure, so we expect the pore fluid remained a single phase.

2.3. Experimental procedure

Thermally cracked dunite cylinders were jacketed in 127 μm thick copper foil and outfitted with foil [strain gages](#), then vacuum saturated with de-ionized water. Instrumented samples were loaded into a triaxial deformation apparatus with a [confining pressure](#) of 15 MPa and a pore [fluid pressure](#) of 10 MPa, resulting in an effective confining pressure of 5 MPa. Once at pressure, the sample and vessel were heated to 150 $^\circ\text{C}$ using an external heater, with a [thermal stability](#) of ± 1 $^\circ\text{C}$ throughout the duration of the experiment. When the assembly reached thermal stability, the sample and all the plumbing was flushed with the chosen pore fluid for the experiment, de-ionized water or CO_2 -rich solution.

For the long hydrostatic pressing experiments, samples were then allowed to react under [hydrostatic pressure](#) for 7 d. Strain data were collected every minute and permeability measurements were made using the transient analysis method ([Boitnott, 1997](#)) every half-hour for the duration of the experiment. Pore fluid aliquots were collected in Teflon vials periodically from the downstream side of the sample, acidified to prevent precipitation, and analyzed for major [cations](#) using an ICP-OES.

For the triaxial deformation experiments, samples were allowed to react under hydrostatic pressure for ~ 72 h. Strain data were collected every minute during the hydrostatic portion of the test. Permeability measurements were taken twice daily. After 3 days of hydrostatic confinement, constant [strain-rate](#) triaxial deformations were performed on the samples at a nominal strain rate of 10^{-5}s^{-1} . Stress and strain data were collected at a frequency of 0.5 Hz during the triaxial deformation and permeability tests were run approximately every 30 MPa of differential stress.

After experiments, samples were dried, a small portion was cut off for unpolished [SEM](#) analysis, and the remaining sample was epoxy impregnated and ground into doubly polished thin sections for optical and SEM inspection. Samples prepared for SEM analysis were sputter coated with approximately 5 nm of [Iridium](#) and affixed to mounts with copper tape. SEM analyses of doubly polished thin sections were

performed on a JEOL JXA 8900R Microprobe at 15 kV accelerating [voltage](#) and analyses of unpolished samples were performed on a Zeiss Auriga FIB-SEM between 3–5 kV accelerating voltage.

3. Results

3.1. Long hydrostatic experiments

During all long [hydrostatic](#) experiments, the sample saturated with CO₂-rich solution shows reduced compaction, enhanced permeability reduction and different [ion concentration](#) evolution compared to the sample saturated with de-ionized water.

Mechanical data from the experiments are presented in [Fig. 1a](#). Both samples show three stages of compaction, an initial rapid phase, a second [quasi-steady state](#) and a third, accelerating stage. The sample saturated with CO₂-rich solution shows similar initial compaction, reduced secondary compaction and an earlier apparent onset of tertiary compaction compared to the sample saturated with de-ionized water.

1. [Download high-res image \(490KB\)](#)
2. [Download full-size image](#)

Fig. 1. Data from long [hydrostatic](#) experiments. Data from experiments with de-ionized water are in blue while data from experiments with carbon-rich solution are in red. Experiments were performed at 150 °C. a) [Volumetric strain](#) versus time; the de-ionized water sample shows more compaction than the carbon-rich solution sample. b) Permeability versus time; the sample saturated with carbon-rich solution has a steeper rate of permeability reduction. Dashed lines are log linear fits to the data. c–f) [Ion concentrations](#) in [pore](#) fluid versus time; trends indicate early [olivine](#) dissolution and later [secondary mineral](#) precipitation. (For interpretation of the references to color in this figure legend, the reader is referred to the web version of this article.)

Although the sample saturated with carbon-rich solution exhibits reduced total compaction, the rate of permeability reduction is higher than that of the sample saturated with de-ionized water, as shown in [Fig. 1b](#). Both samples have a log linear reduction in permeability over the course of experiments, with no apparent direct correlation with compaction rate.

Ion concentrations (Mg^{2+} , Si^{4+} , Ca^{2+} , Fe^{2+}) in [pore](#) fluid evolve differently during hydrostatic pressing for samples with the two pore fluids. Chemical data from time-series fluid aliquots are presented in [Fig. 1c–f](#). The pore fluid from the sample saturated with carbon-rich solution shows an early spike and decay in Mg^{2+} , while the Si^{2-} in the pore fluid increases for ~50 h before beginning to decrease. Ca^{2+} appears to remain flat for the duration of the experiment and Fe continuously increases. Pore fluid from the sample saturated with de-ionized water shows Mg^{2+} and Si^{4+} increase for ~50 h before beginning to decrease and no systematic trend in Ca^{2+} or Fe^{2+} .

3.2. Short hydrostatic experiments

[Bicarbonate](#) concentration in pore fluid and temperature both appear to have an effect on the compaction of dunites. Mechanical data from all short hydrostatic experiments are presented in [Fig. 2a](#). All experiments were performed with 10 MPa [pore pressure](#) and 15 MPa [confining pressure](#) at room temperature or 150 °C. The sample saturated with de-ionized water at room temperature shows the least compaction, under 0.01% total volumetric reduction. The sample saturated with de-ionized water at elevated temperature shows the most initial compaction, but is overtaken at ~55 h by the sample saturated with the 0.6 M NaHCO_3 solution. The sample saturated with the 0.6 M NaHCO_3 solution shows slightly reduced compaction compared to the de-ionized water sample at elevated temperature at the beginning of the experiment, but the compaction rate increases toward the end of the experiment. The sample saturated with

the 1.5 M NaHCO₃ solution shows a further reduction in compaction compared to the low bicarbonate and de-ionized water samples.

1. [Download high-res image \(236KB\)](#)
2. [Download full-size image](#)

Fig. 2. Data from short [hydrostatic](#) experiments. Data from experiments with de-ionized water at room temperature are in cyan, de-ionized water at elevated temperature are in blue, carbon-rich solution with 0.5 M NaHCO₃ are in red and carbon-rich solution with 1.5 M NaHCO₃ are in green. Experiments at elevated temperature were performed at 150 °C. a) [Volumetric strain](#) versus time. The room temperature sample shows little compaction, while samples at elevated temperature compact for the entire duration of the experiment. Initial compaction appears to anti-correlate with [bicarbonate](#) concentration. Samples saturated with carbon-rich solution show a late increase in compaction rate. Vertical lines are signals from permeability tests. b) Permeability versus time; variation in permeability is small, but the extent of permeability reduction appears to correlate with [pore](#) fluid bicarbonate concentration. (For

interpretation of the references to color in this figure legend, the reader is referred to the web version of this article.)

Permeability is reduced over the duration of experiments for all pore [fluid compositions](#). Permeability data from short hydrostatic experiments are presented in [Fig. 2b](#). Changes in permeability for the de-ionized water sample at room temperature are small. Among elevated temperature samples, there is the suggestion of an anti-correlation between permeability reduction and pore fluid bicarbonate concentration, but variability is small.

3.3. Triaxial deformation experiments

Pore fluid composition and temperature have a strong effect on the deformation behavior and strength of [dunite](#). Samples with 3 different pore fluids were deformed triaxially after three days of hydrostatic pressing. Mechanical data are presented in [Fig. 3a–b](#). When differential stress is plotted against [axial strain](#) ([Fig. 3a](#)), all samples show four stages of deformation, an initial compaction phase of the closure of oriented pre-existing cracks, a second phase of the quasi-elastic behavior, a third phase of [strain softening](#) and dilation and final phase of shear failure after the peak stress. Effective [Young's Modulus](#) is calculated from the second stage. All samples fail by localized brittle faulting.

1. [Download high-res image \(414KB\)](#)
2. [Download full-size image](#)

Fig. 3. Data from triaxial deformation experiments. Coloring is the same as for short [hydrostatic](#) experiments. a) Differential stress versus axial [strain](#). The room temperature sample has the greatest [shear strength](#), while the de-ionized water sample at elevated temperature has the lowest shear strength. Samples saturated with carbon-rich solution have lower apparent [Young's moduli](#) but intermediate shear strength. b) [Volumetric strain](#) versus [axial strain](#); samples saturated with carbon-rich solution accommodate more axial strain before dilating. Vertical lines are signals from permeability tests. c, d) Permeability versus strain. All samples exhibit permeability reductions during triaxial deformation. The samples saturated with de-ionized water and 0.6 M NaHCO₃ solution at elevated temperature show slight permeability enhancements near the time of failure.

The sample saturated with de-ionized water at room temperature has the highest Young's modulus, at 55.6 GPa, as well as the highest peak stress, 175 MPa. The sample saturated with de-ionized water at elevated temperature is less stiff, with a Young's modulus of 34.5 GPa, 38% lower than at room temperature, and has the lowest peak stress, 104 MPa, a 41% reduction relative to the sample reacted at room temperature. Samples saturated with carbon-rich solution show an even further reduction of Young's modulus, but attained higher peak stress than the de-ionized water sample at elevated temperature. The sample saturated with the 0.6 M NaHCO₃ solution has a Young's modulus of 28.7 GPa and a peak stress of 146 MPa. The sample saturated with the 1.5 M NaHCO₃ solution has a Young's modulus of 31.7 GPa and a peak stress of 150 MPa. A summary of these mechanical data is presented in [Table 1](#). Additional experiments were run to assess repeatability with good agreement, the data from which is presented in Supplementary Figure S2 and summarized in Supplementary Table 1.

Table 1. Summary of mechanical data from all [triaxial tests](#).

| Name | Temp (°C) | Fluid composition | Hydrostatic duration (Hr) | Strength (MPa) | E (GPa) |
|---------------------------|------------------|--|----------------------------------|-----------------------|----------------|
| DUN-1 | 23 | DW | 0 | 167 | 48.5 |
| DUN-7 | 150 | DW | 180 | NA | NA |
| DUN-8 | 150 | 0.6 M NaHCO ₃ , CO ₂ | 180 | NA | NA |
| DUN-11^a | 150 | DW | 24 | NA | 38.9 |
| DUN-15^a | 150 | 0.6 M NaHCO ₃ , CO ₂ | 24 | NA | 31.1 |
| DUN-18 | 150 | DW | 72 | 104 | 34.5 |
| DUN-19 | 23 | DW | 72 | 175 | 55.6 |
| DUN-23 | 150 | 1.5 M NaHCO ₃ , CO ₂ | 72 | 150 | 31.7 |
| DUN-24 | 150 | 0.6 M NaHCO ₃ , CO ₂ | 72 | 146 | 28.7 |

a

Samples not taken to failure.

All samples show reductions in permeability during triaxial deformation. Permeability data collected during deformation is presented in [Fig. 3c–d](#). The sample saturated with de-ionized water at room temperature has the highest initial permeability and shows the greatest reduction in permeability during triaxial deformation. The sample saturated with de-ionized water at elevated temperature and the samples saturated with the CO₂-rich solution show reductions in permeability until close to peak stress, when permeability increases slightly, likely indicating coalescence of [microcracks](#).

3.4. Reaction path model

The Geochemist Workbench (GWB) software ([Bethke, 2008](#)) was used for reaction path modeling (React module). Reaction path modeling was used to predict solution composition, shifts in pH, and mineral saturation as a function of reaction progress. The simulations involved two steps: (1) equilibrating NaHCO₃ solution with added CO₂ at room temperature (following the experimental sequence), and then (2) adding the reactants (forsterite Mg₂SiO₄ and [fayalite](#) Fe₂SiO₄) into the aqueous system at 423 K (150 °C).

The solubility of CO₂ in NaHCO₃ solutions decreases with increasing temperature ([Han et al., 2011](#)), therefore to account for this decrease in solubility, we allowed the pH to drift from the original value of 6.0–6.5 to pH 7.0 in the reaction path models. In addition to NaHCO₃ components present in the synthetic brine, we also specified the concentration of calcium (Ca²⁺), since this element was consistently detected in DW (~4 ppm Ca²⁺) and NaHCO₃ (~8 ppm Ca²⁺) experiments, likely from dissolution of trace [diopside](#). Kinetic rate parameters were specified for mineral dissolution, while relevant minerals were allowed to precipitate instantaneously.

For the initial models, at 423 K the kinetic dissolution constants were set at $1.2 \times 10^{-11} \text{ mol cm}^{-2} \text{ s}^{-1}$ for all reactors ([Hänchen et al., 2006](#)). The duration of the reaction was set at 200 h. We used the Lawrence Livermore National Laboratory (LLNL) *thermo.dat* database included in the GWB package. The CO₂ solubility in NaHCO₃ solutions was calculated using modified Setschenow equation reported in [Han et al. \(2011\)](#). The calculated CO₂ solubility at a *p*CO₂ of 5.1 MPa at room temperature is 0.85 mol kg⁻¹ for 0.6 M NaHCO₃, and 0.36 mol kg⁻¹ for 1.5 M NaHCO₃. The solid to liquid ratio in the models was matched to that of the experiment, taking into account that average porosity of samples was 1%. The mineral reactive surface area was set at 0.01 cm³ g⁻¹, a typical value for thermally cracked [crystalline rocks](#) ([Darot et al., 1992](#)). The solid phases that cannot form at the conditions of our experiments (e.g. [quartz](#) SiO₂, and [tridymite](#) SiO₂) were suppressed in the models. Additionally, we suppressed [dolomite](#) CaMg(CO₃)₂ as dolomite was not observed in the experiments. The initial models were run using the dissolution rate reported in the literature ([Table 1](#)). The results are shown in [Fig. 4](#). Silicon, magnesium, and iron are predicted to be released during the dunite dissolution in the DW and NaHCO₃ reactors. In the DW reactor, the primary alteration phases predicted to form on the timescale of this experiment are antigorite [serpentine](#) ((Mg, Fe)₃Si₂O₅(OH)₄) and [brucite](#) (Mg(OH)₂). In the 0.6 M and 1.5 M NaHCO₃ reactors, the predicted alteration phases are [magnesite](#) (MgCO₃), [calcite](#) (CaCO₃) and [siderite](#) (FeCO₃). While these modeling results capture the observed trend, namely when de-ionized water reactor is compared

to the 0.6 M NaHCO₃ reactor, the solubility of silicon, magnesium and iron are higher in the NaHCO₃ reactor, the absolute predicted concentrations are considerably (~20–500 times) lower than the observed concentrations. This indicates that the apparent dissolution rate in our systems is significantly higher than the reported rate for the dissolution of [olivine](#) ([Hänchen et al., 2006](#)).

1. [Download high-res image \(301KB\)](#)
2. [Download full-size image](#)

Fig. 4. a, b) Chemical analysis of [effluent](#) fluid presented with results of a reaction path simulation from Geochemist's Workbench. Curves in red are CO₂-rich experiments and simulations while blue curves are from experiments and simulations with de-ionized water. Large circles are experimental data, dashed lines are from simulations with fast reaction rates, and dotted lines are from simulations with slow reaction rates. a) Mg versus time and b) Si versus time. c–e) Results of a reaction path simulation from Geochemist's Workbench. c) Minerals predicted to precipitate in the CO₂-rich experiments, d) same with [magnesite](#) suppressed, and e) minerals predicted to precipitate in de-ionized water experiments. (For interpretation of the references to color in this figure legend, the reader is referred to the web version of this article.)

To estimate the apparent dissolution rate in our systems, we ran several models while varying the dissolution rate, and found that the dissolution rate of $3.16 \times 10^{-9} \text{ mol cm}^{-2} \text{ s}^{-1}$ results in the order of magnitude agreement with the observed aqueous concentrations. This value was used to construct a second set of reaction path models (dashed lines in [Fig. 4a, b](#)). Similar to the slow dissolution rate models, silicon, magnesium, and iron are predicted to be released during the dunite dissolution, and the predicted alteration phases are the same – brucite and antigorite for the DW system, and calcite, magnesite, and siderite for the NaHCO₃ reactors; however, the absolute amounts of the secondary phases predicted to precipitate are orders of magnitude larger ([Fig. 4c, e](#)).

In all experiments at elevated temperature, we observed the formation of a minor amount of serpentine phase lizardite Mg₃Si₂O₅(OH)₄ ([Fig. 5](#)). Lizardite is not included in the *thermo.dat* database, so data for antigorite was used. The geochemical modeling predicts formation of a serpentine phase in the DW reactor only; however, in the carbonate-rich NaHCO₃ reactors, magnesite is the only Mg-containing phase predicted to precipitate. When the formation of magnesite is suppressed in the models with fast dissolution rate, serpentine is predicted to form in the 0.6 M and 1.5 M NaHCO₃ reactors. This is due to the non-instantaneous [nucleation](#) of magnesite. [Giammar et al., 2005](#) reported that nucleation of magnesite is the rate-limiting step during magnesite precipitation, and a critical saturation index between 0.25 and 1.14 is required for temperature of 95 °C and CO₂ pressure of 10.0 MPa ([Giammar et al., 2005](#)). The retarded nucleation of magnesite will lead to locally high Mg²⁺, allowing for the precipitation of serpentine ([Fig. 4d](#)). A summary of the inputs for the models is presented in Supplementary Table 2.

1. [Download high-res image \(677KB\)](#)
2. [Download full-size image](#)

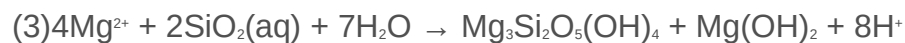
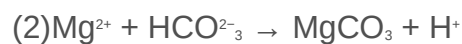
Fig. 5. [SEM](#) images of crack surfaces split along pre-existing cracks (insert) of samples from long [hydrostatic](#) experiments. a) Unreacted sample, in which [olivine](#) surfaces have

angular features and no secondary mineralization. b) Overview of crack surface from sample saturated with de-ionized water, in which [serpentine](#) was precipitated along olivine surface. c) Close-up of de-ionized water sample, in which serpentine precipitated as elongate fin-like sheets and appears to be porous and permeable. d) Overview of crack surface from sample saturated with carbon-rich solution, in which serpentine and [magnesite](#) intergrow across the olivine grain surface. e) Close up of sample saturated with carbon-rich solution, in which serpentine and magnesite layers appear to be porous. f) Serpentine and magnesite layers are discontinuous, leaving some fresh olivine surfaces bare. g) Serpentine and magnesite layers appear to be cracked, which is another possible mechanism allowing continuous fluid access to the unreacted olivine.

4. Discussion

4.1. Evolution of pore fluid chemistry

Differences in the evolution of [ion concentration](#) in [pore](#) fluid during long [hydrostatic](#) experiments point to different dissolution–precipitation dynamics. The reactions occurring while [olivine](#) is hydrated and carbonated can be approximated as



where the dissolution of [forsterite](#) releases Mg^{2+} and SiO_2 into solution, the precipitation of [magnesite](#), [serpentine](#) and [brucite](#) remove Mg^{2+} from solution and the precipitation of serpentine removes SiO_2 from solution. The precipitation of amorphous [silica](#) (from the dissolved silica) could also remove SiO_2 from solution.

Samples saturated with both de-ionized water and carbon-rich solution show an early spike in both Mg^{2+} and Si^{4+} ([Fig. 4a, b](#)), indicating that dissolution begins rapidly at the beginning of experiments. From here the evolution of the ion concentration in the two pore fluids diverges. The model in [Fig. 4](#) shows that rapid magnesite precipitation begins immediately upon forsterite dissolution, due to the reactivity of the dissolved Mg^{2+} and CO_2 . This is likely responsible for the drop in Mg^{2+} measured in the pore fluid of the carbon-rich solution sample. In the de-ionized water sample, Mg^{2+} continues to rise for ~ 50 h, indicating that forsterite dissolution outpaces any secondary mineralization. Si^{4+} continues to rise in both pore fluids for ~ 50 h, then is reduced continuously, likely the result of the later precipitation of serpentine as shown in the reaction path model. It should be noted as well that in addition to the divergence in pore fluid chemistry evolution, the sample saturated with carbon-rich solution has a larger magnitude of

dissolved [cations](#) for the entire duration of the experiment, indicating that dissolution is more vigorous in that sample. Although the reaction path models qualitatively reproduce the [chemical evolution](#) of our pore fluid, the differences between the observations and the model underscore the difficulty in applying reaction rates gleaned from powder reactor studies to real rocks with complex pore geometries. It is possible that the elevated normal stress experienced by [asperities](#) along fracture surfaces in the sample under stress leads to higher than expected dissolution rates.

4.2. Effect of carbon-rich solution

The observed pore fluid chemistry change and predicted the reaction path model are consistent with the reaction [microstructures](#) produced during the experiments. [SEM](#) images of unpolished crack walls are presented in [Fig. 5](#). Pristine sample material is entirely olivine, with angular surfaces free of dissolution features and [secondary minerals](#) ([Fig. 5a](#)). The sample saturated with de-ionized water ([Fig. 5b, c](#)) shows rounding of edges and precipitation of serpentine along crack walls. Serpentine appears to grow in elongated flakes and remains porous, suggesting maintenance of fluid access to reactive surfaces. The sample saturated with CO₂-rich solution shows more substantial secondary mineralization ([Fig. 5d–f](#)). Serpentine and magnesite are intergrown in porous layers along the crack walls. The mineralized layers appear discontinuous along the crack wall and have cracks that appear to have formed in-situ because of mineral growth within them ([Fig. 5f](#)). The layers do not appear to entirely block fluid access to reactive material and may be acting as “proppants”, keeping cracks open. This is consistent with the reduced compaction accompanied by increased permeability reduction seen in the samples saturated with reactive fluid. Secondary mineralization leads to a less compressible [pore space](#), slower dissolution of asperities and smaller [fracture apertures](#).

The [bicarbonate](#) concentration of the CO₂-rich solution has an effect on the magnesite and serpentine precipitation textures. [SEM](#) images of precipitates from the CO₂-rich solution samples are presented in [Fig. 6](#). The low bicarbonate sample shows a larger contribution of dissolution, with ubiquitous etch pits and cave-like, surface-intersecting cracks. Magnesite and serpentine are intergrown in sparse patches, leaving patches of olivine uncovered. The high bicarbonate sample has all of its olivine surfaces covered in secondary minerals, with olivine only apparent through cracks in the mineralized layer ([Fig. 6b](#)). These cracks sometimes have precipitants in them, suggesting that they form during experiments and are not [decompression](#) fractures that formed during unloading.

Magnesite tends to precipitate as compound [crystals](#) with many facets, although some well-formed [single crystals](#) are observed ([Fig. 6f–h](#)).

1. [Download high-res image \(970KB\)](#)
2. [Download full-size image](#)

Fig. 6. [SEM](#) images of samples saturated with carbon-rich solution from triaxial experiments. Higher [bicarbonate](#) concentration appears to lead to an enhancement in carbonate precipitation and a modification of precipitation morphology. a, c, e, g) Sample saturated with 0.6 M NaHCO_3 solution, in which dissolution features are dominant and [magnesite](#) tends to grow as well-terminated [polyhedra](#) or coarse aggregate [crystals](#). b, d, f, h) Sample saturated with 1.5 M NaHCO_3 solution, in which precipitation is much more prominent, with most surfaces completely armored. Magnesite tends to grow as complex aggregate crystals.

The modest reduction in permeability displayed by samples can be explained by the evolution of the pore structure throughout reaction. Examination of traditional double-polished thin sections shows that carbon rich fluid enhances the dissolution of olivine as well as precipitation of secondary minerals. SEM backscattered electron images of polished thin sections are presented in [Fig. 7](#). Samples saturated with de-ionized water show some alteration and nascent etch pits can be seen along crack surfaces ([Fig. 7a](#)). Etch pits appear to have coalesced and broken pieces of coherent grain off into cracks ([Fig. 7b](#)). Secondary mineralization is present, but in thin layers ($<1 \mu\text{m}$) that are close to the resolution of the SEM used for this analysis.

1. [Download high-res image \(415KB\)](#)
2. [Download full-size image](#)

Fig. 7. [SEM](#) images of polished thin sections of samples from long [hydrostatic](#) experiments. a, b) Sample saturated with de-ionized water. Alteration is focused around crack walls and mostly consists of dissolution features. [Secondary minerals](#) are not apparent at this scale. c, d) Sample saturated with carbon-rich solution.

Alteration is more substantial. Dissolution channelized into etch pits which coalesce at a distance beneath primary crack surfaces, perforating the crack walls. Secondary minerals are the dark grey material within cracks.

Samples saturated with the CO₂-rich solution show much more substantial alteration.

Etch pits are apparent along all crack surfaces, and appear to grow in oriented, parallel bands ([Fig. 7c](#)), suggesting some influence of stress or crystallographic orientation.

Dissolution channels tend to perforate the crack surface and coalesce at some distance beneath the pre-existing cracks, which ultimately separate the altered surface from the rest of the intact grain ([Fig. 7d](#)). Such layered alteration may be the onset of the

hierarchical fractures or kernel patterns commonly observed in metasomatised rocks ([Iyer et al., 2008](#), [O'Hanley, 1992](#)).

Secondary mineralization is ubiquitous on altered surfaces in layers 1 to ~10 µm thick, but was difficult to characterize in polished thin sections. In order to take a look at the secondary minerals in greater detail, unpolished samples broken along pre-existing cracks were imaged to inspect the crack walls.

Microstructures from triaxial deformation tests, following a short period of hydrostatic pressing, highlight the interaction of chemical reaction and mechanical deformation.

SEM images of crack walls of unpolished samples from triaxial experiments are presented in [Fig. 8](#). Surface intersecting cracks are imaged to highlight the penetration of reactive fluids into the olivine. Differences in reaction microstructures among samples saturated with different fluids and under different conditions provide insight into variations in mechanical behavior.

The sample saturated with de-ionized water at room temperature shows the least alteration ([Fig. 8a](#)). Undulations in surface intersecting cracks indicate nascent etch pits, but that is the only apparent alteration feature. The sample saturated with de-ionized water at elevated temperature shows more developed dissolution features ([Fig. 8b](#)).

Etch pits form and begin to coalesce a small distance from the surface of the crack. Some serpentine is observed precipitated along the crack wall. The sample saturated with low bicarbonate CO₂-rich solution shows much more substantial alteration ([Fig. 8c](#)).

Dissolution features tend to be prominent and channelized. Etch pits form an interconnecting network that coalesces at a distance

from pre-existing crack surfaces, perforating the olivine. Magnesite and serpentine are both observed precipitated on crack walls, but appear porous and have not grown to entirely cover the surface, leaving patches of olivine exposed for further reaction. The sample saturated with high bicarbonate-solution shows more precipitation than the low bicarbonate sample ([Fig. 8d](#)).

Surfaces appear armored with porous magnesite and serpentine intergrowths. Mechanical data from the hydrostatic portion of the experiment

indicate that compaction had not ceased by the end of the experiment, suggesting that this porous layer is permeable, maintaining fluid communication with reactive surfaces.

1. [Download high-res image \(619KB\)](#)

2. [Download full-size image](#)

Fig. 8. [SEM](#) images of crack surfaces split along pre-existing cracks (insert) of samples from short [hydrostatic](#) experiments. Surface intersecting cracks are imaged to highlight fluid penetration. a) Sample saturated with de-ionized water at room temperature, in which crack shows little alteration. b) Sample saturated with de-ionized water at elevated temperature, in which crack shows incipient etch pits. c) Sample saturated with 0.6 M NaHCO_3 solution, in which crack shows extensive dissolution features and secondary mineralization. d) Sample saturated with 1.5 M NaHCO_3 solution, in which secondary mineralization is so dense that crack surface is no longer visible. e) [Microcracks](#) radiating out of etch pits in sample saturated with de-ionized water at elevated temperature. This enhancement of microcracking may explain the low [shear strength](#) of the sample.

4.3. Effect of differential stress

[Hydrothermal alteration](#) of the [dunite](#) samples leads to modification of their mechanical behavior. A summary of mechanical results is presented in [Table 1](#) and images of polished thin sections are presented in [Fig. 9](#). All samples failed by localized [brittle fracture](#). Inspection of petrographic thin sections indicates that failure localized due to the interaction and coalescence of [microcracks](#). The sample saturated with de-ionized water at room temperature has the highest [shear strength](#) and [Young's modulus](#). SEM analysis shows that the sample shows very little alteration during the deformation test ([Fig. 8a](#)), so can be considered a control case for chemo-mechanical coupling. The sample saturated with de-ionized water at elevated temperature, in which dissolution features such as etch pits are observed ([Fig. 8b](#)), has the lowest shear strength, with a reduction of 41% compared to the control case, but intermediate Young's modulus. Macroscopic inspection of the post-failure sample shows a well developed, through-going shear fracture ([Fig. 9b](#)). The pre-existing cracks are primarily along [grain boundaries](#), leading to enhanced alteration of grain contacts, where most of the microcracking occurs. The reduction of shear strength may be explained by the presence of etch pits, which may serve as stress concentrators and lower the stress required to fracture the rock. Microstructural observations corroborate this interpretation, as microcracks can be seen radiating out from the etch pits ([Fig. 8d](#)). There are other mechanisms that may result in the observed weakening as well, including subcritical [cracking](#) and precipitation of weak minerals along grain boundaries. The total observed effect is likely a combination of several of these mechanisms operating at once. Precipitation of serpentine along crack surfaces may account for the reduction in apparent Young's modulus at low stress levels, before the onset of microcracking.

1. [Download high-res image \(921KB\)](#)
2. [Download full-size image](#)

Fig. 9. Scanned images of polished thin sections of samples from triaxial deformation experiments. a) Sample saturated with de-ionized water at room temperature shows significant microcracking. A localized fracture is observed on top half of the sample. b) Sample saturated with de-ionized water at elevated temperature shows sharp through going shear fractures. c) Sample saturated with 0.6 M NaHCO₃ solution appears to have more distributed shear fractures throughout. d) Sample saturated with 1.5 M NaHCO₃ solution shows evidence for well-formed distributed shear fractures throughout. Samples saturated with CO₂-rich solution have intermediate strength between the room temperature and elevated temperature de-ionized water samples and the lowest Young's moduli. Precipitation of serpentine and magnesite along crack surfaces again manifests as a reduction in apparent Young's modulus at low stress levels. This mechanism is also consistent with the observed enhancement of non-linear stress-strain behavior at very low differential stress ([Fig. 3a](#)). This stage of deformation is typically ascribed to the closure of optimally oriented cracks ([Walsh, 1965](#)), and its enhancement suggests that these cracks have become more compliant after reaction. The sample etch pit [nucleation](#) mechanism may be operating in these samples, but slightly tempered by the reduction in total porosity due to precipitation. It is likely that some subcritical cracking takes place during the hydrostatic portion of tests, and this may also explain some of the mechanical differences. Previous work has shown that

subcritical crack growth in basic rocks is sensitive to the activity of water at crack tips ([Meredith and Atkinson, 1985](#)), which may explain why DI samples show more weakening than samples saturated with CO₂-rich solutions with a lower water activity. Furthermore, compliant secondary minerals may also dissipate stress along crack surfaces by [plastic deformation](#) of weak [phyllosilicates](#) rather than fracturing. Armoring of surfaces by secondary minerals hampered observation of microcracking at very fine scale. Macroscopic observation of post-failure samples shows the development of several distributed shear fractures, suggesting that hydrothermal alteration encourages distributed over localized deformation at the sample scale.

4.4. CO₂ injection into reactive reservoirs

The mechanical response of reservoirs to injection and depletion has been studied mostly with regard to poroelastic effects (e.g. [Grasso, 1992](#)), some of which may be affected by the changes in mechanical characteristics observed in this study. Changes in the [pore pressure](#) of porous reservoirs have been observed to result in faulting and [seismicity](#) ([Zoback and Zinke, 2002](#)) as has been highlighted by recent episodes of seismicity that result from [wastewater](#) storage ([Ellsworth, 2013](#)). Injection into reservoirs can lead to pore pressure overpressurization and hydrofracture; depletion can lead to [subsidence](#) and evolution of reservoir stress state towards failure. Both these behaviors are the result of changes in pore pressure as a result of increasing or reducing the volume of water in the pore space, but could also be accomplished by changing the volume of pore space itself. It has been noted that CO₂ storage may be less likely to trigger earthquakes due to reductions in [overpressure](#) from CO₂ dissolution into brine and the subcritical stress state of sedimentary reservoirs ([Vilarrasa and Carrera, 2015](#)), but these conclusions do not apply to low porosity mafic and ultramafic reservoirs. Changes in pore pressure may also result from a reduction in pore volume due to precipitation, or an increase in pore volume due to dissolution. In addition, the feedback between injection and pore pressure may be further complicated by the alteration of crack walls. Studies have shown that compliant pore walls can amplify the effect pore pressure has on the relationship between [effective stress](#) and permeability ([Zoback and Byerlee, 1975](#)). Experimental and modeling studies of the injection of CO₂ into carbonate caprocks indicate that dissolution can lead to a net increase in pore space ([Luquot and Gouze, 2009](#), [Gauss et al., 2005](#)), but the model did not take specific micromechanisms such as channelized dissolution into account, and may underpredict mechanical feedbacks.

If major projects to inject CO₂ into reservoirs of [ultramafic and mafic rocks](#) proceed, a greater understanding of the coupling between [chemical alteration](#) and mechanical

deformation is advisable. The precipitation of compliant minerals along crack surfaces may result in not only reservoir compaction and subsidence, but may affect the frictional behavior of pre-existing faults in the reservoir, influencing [seismic hazard](#), a topic that warrants more investigation. Dissolution of minerals may result in not only compaction and subsidence, but may encourage microcracking by concentrating stress. Cracking is a dilatant process, which increases total porosity, which may play a role in maintaining permeability and reactive surface area in reservoirs, but may also result in rupture and seismicity.

5. Conclusions

We performed [hydrostatic](#) compaction and triaxial deformation experiments on dunites under hydrothermal and CO₂-rich conditions. [Shear strength](#), [Young's modulus](#), permeability and sample [porosity](#) are all reduced during reaction. The evolution of physical properties of dunites reacted with water and CO₂ is complex and controlled by chemo-mechanical coupling. Analysis of mechanical, chemical and microstructural data suggests that the hydrostatic compaction behavior of the [dunite](#) samples is controlled by dissolution of [olivine](#) and the precipitation of [secondary minerals](#) such as [serpentine](#) and [magnesite](#) along pre-existing cracks. Layers of secondary minerals precipitated on crack walls are porous and allow continuous fluid-mineral contact. Alteration layers are no thicker than tens of microns, but occur along [grain boundaries](#) and so have substantial effects on the deformation behavior of the samples, causing considerable reduction in apparent elastic moduli and shear strength. Reduction of Young's modulus appears to be the result of secondary mineralization along crack surfaces while reduction in strength may be the result of the intensification of stress at channelized dissolution features. Dissolution rates observed are greater than those published in the literature for powder reactors, suggesting stress enhanced dissolution. A greater understanding of this evolution is advisable for the safety and success of any future ultramafic or mafic [carbon dioxide](#) mineralization sites, and to better constrain the dynamics of deformation and [hydrothermal alteration](#) of the [oceanic crust](#).

Acknowledgments

The work of HL and WZ was supported by the U.S. Department of Energy, Office of Science, the Office of Basic Energy Sciences, Chemical Sciences, Geosciences, & Biosciences Division under Award Number [DE-FG-0207ER15916](#) and by the Office of Science, National [Energy Technology](#) Laboratory under Award Number [DE-FE-](#)

[0004375](#). Geochemical modeling by AI is supported as part of the Center for Frontiers in Subsurface Energy Security, an Energy Frontier Research Center funded by the U.S. Department of Energy(DOE), Office of Science, Basic Energy Sciences (BES), under Award # [DE-SC0001114](#) at Sandia National Laboratories. Sandia National Laboratories is a multi-mission laboratory managed and operated by Sandia Corporation, a wholly owned subsidiary of Lockheed Martin Corporation, for the U.S. Department of Energy's National Nuclear Security Administration under contract [DE-AC04-94AL85000](#). HL would like to thank the Graduate School at the University of Maryland, College Park for the additional support of the Wylie Fellowship. We benefit from discussions with B. Evans, R. Cooper and G. Hirth during early stages of this project. We thank Y. Fei for access of the FIB-SEM facility; K. Crispin and E. Bullock for assistance with FIB-SEM analyses; A. Beinlich for assistance with ICP-OES analyses; P. Piccoli for assistance with [electron microprobe](#) analyses; K. Miller for assistance with 3D data analysis; and G. Boitnott, J. Noel and T. Tamarkin for the technical support for the deformation apparatus.

This manuscript benefits greatly from the thoughtful reviews of Matej Pec and an anonymous reviewer.

Appendix A. Supplementary material

The following is the Supplementary material related to this article.

[Download Word document \(571KB\)Help with docx files](#)

MMC 1. Experimental details.

References

[Andreani et al., 2009](#)

Muriel Andreani, L. Luquot, P. Gouze, M. Godard, E. Hoisé, B. Gibert **Experimental study of carbon sequestration reactions controlled by the percolation of CO₂-rich brine through peridotites**

Environ. Sci. Technol., 43 (4) (2009), pp. 1226-1231

[CrossRefView Record in Scopus](#)

[Bethke, 2008](#)

C. Bethke **Geochemical and Biogeochemical Reaction Modeling**

Cambridge University Press, Cambridge, UK (2008)

[Boitnott, 1997](#)

G.N. Boitnott **Use of complex pore pressure transients to measure permeability of rocks**

Proceedings of SPE Annual Technical Conference and Exhibition, San Antonio, Texas, 5–8
October 1997(1997)

[Chen et al., 2006](#)

Z.-Y. Chen, W.K. O'Connor, S.J. Gerdemann **Chemistry of aqueous mineral carbonation for
carbon sequestration and explanation of experimental results**

Environ. Prog., 25 (2) (2006), pp. 161-166

<http://doi.org/10.1002/ep.10127>

[ArticleDownload PDF](#)[CrossRefView Record in Scopus](#)

[Darot et al., 1992](#)

M. Darot, Y. Gueguen, M. Baratin **Permeability of thermally cracked granite**

Geophys. Res. Lett., 19 (1) (1992), p. 869

[CrossRefView Record in Scopus](#)

[Daval et al., 2011](#)

D. Daval, O. Sissmann, N. Menguy, G.D. Saldi, F. Guyot, I. Martinez, R. Hellmann **Influence of
amorphous silica layer formation on the dissolution rate of olivine at 90 °C and
elevated $p\text{CO}_2$**

Chem. Geol., 284 (1) (2011), pp. 193-209

[ArticleDownload PDF](#)[View Record in Scopus](#)

[Demartin et al., 2004](#)

B. Demartin, G. Hirth, B. Evans **Experimental constraints on thermal cracking of peridotite at
oceanic spreading centers**

Mid-Ocean Ridges (2004), pp. 167-185

[View Record in Scopus](#)

[Elkhoury et al., 2013](#)

J.E. Elkhoury, P. Ameli, R.L. Detwiler **Dissolution and deformation in fractured carbonates
caused by flow of CO_2 -rich brine under reservoir conditions**

Int. J. Greenh. Gas Control, 16 (Suppl.) (2013), pp. S203-S215

<http://doi.org/10.1016/j.ijggc.2013.02.023>

[ArticleDownload PDF](#)[View Record in Scopus](#)

[Ellsworth, 2013](#)

W.L. Ellsworth **Injection-induced earthquakes**

Science, 341 (6142) (2013), Article 1225942

[CrossRef](#)

[Gadikota et al., 2014](#)

G. Gadikota, J. Matter, P. Kelemen, A.-H.A. Park **Chemical and morphological changes during
olivine carbonation for CO_2 storage in the presence of NaCl and NaHCO_3**

PCCP, Phys. Chem. Chem. Phys., 16 (10) (2014), pp. 4679-4693

<http://doi.org/10.1039/c3cp54903h>

[CrossRefView Record in Scopus](#)

[Gauss et al., 2005](#)

I. Gauss, M. Azaroual, I. Czernichowski-Lauriol **Reactive transport modelling of the impact of CO₂ injection on the clayey cap rock at Sleipner (North Sea)**

Chem. Geol., 217 (3) (2005), pp. 319-337

[Giammar et al.,
2005](#)

D.E. Giammar, R.G. Bruant, C.A. Peters **Forsterite dissolution and magnesite precipitation at conditions relevant for deep saline aquifer storage and sequestration of carbon dioxide**

Chem. Geol., 217 (2005), pp. 257-276

[ArticleDownload PDFView Record in Scopus](#)

[Godard
et al.,
2013](#)

M. Godard, L. Luquot, M. Andreani, P. Gouze **Incipient hydration of mantle lithosphere at ridges: a reactive-percolation experiment**

Earth Planet. Sci. Lett., 371–372 (2013), pp. 92-102

<http://doi.org/10.1016/j.epsl.2013.03.052>

[ArticleDownload PDFView Record in Scopus](#)

[G
r
a
s
s
o
-
1
9
9
2](#)

J.R. Grasso **Mechanics of seismic instabilities induced by the recovery of hydrocarbons**

Pure Appl. Geophys., 139 (3–4) (1992), pp. 507-534

<http://doi.org/10.1007/BF00879949>

[CrossRefView Record in Scopus](#)

[Guyot et
al., 2011](#)

F. Guyot, D. Daval, S. Dupraz, I. Martinez, B. Ménez, O. Sissmann **CO₂ geological storage: the environmental mineralogy perspective**

C. R. Géosci., 343 (2–3) (2011), pp. 246-259

<http://doi.org/10.1016/j.crte.2010.12.007>

[ArticleDownload PDFView Record in Scopus](#)

[Han et al., 2011](#)

X. Han, Z. Yu, J. Qu, T. Qi, W. Guo, G. Zhang **Measurement and correlation of solubility data for CO₂ in NaHCO₃ aqueous solution**

J. Chem. Eng. Data, 56 (2011), pp. 1213-1219

[CrossRefView Record in Scopus](#)

[Hänchen et al., 2006](#)

M. Hänchen, V. Prigiobbe, G. Storti, T. Seward, M. Mazzotti **Dissolution kinetics of forsteritic olivine at 90–150 °C including effects of the presence of CO₂**

Geochim. Cosmochim. Acta, 70 (2006), pp. 4403-4416

[ArticleDownload PDFView Record in Scopus](#)

[Hawkes et al., 2005](#)

C.D. Hawkes, P.J. McLellan, S. Bachu **Geomechanical factors affecting geological storage of CO₂ in depleted oil and gas reservoirs**

J. Can. Pet. Technol., 44 (10) (2005)

[Hövelmann et al., 2012](#)

J. Hövelmann, H. Austrheim, B. Jamtveit **Microstructure and porosity evolution during experimental carbonation of a natural peridotite**

Chem. Geol., 334 (2012), pp. 254-265

<http://doi.org/10.1016/j.chemgeo.2012.10.025>

[ArticleDownload PDF](#)

[Huerta et al., 2012](#)

N.J. Huerta, M.A. Hesse, S.L. Bryant, B.R. Strazisar, C.L. Lopano **Experimental evidence for self-limiting reactive flow through a fractured cement core: implications for time-dependent wellbore leakage**

Environ. Sci. Technol., 47 (2012)

[IPCC, 2014](#)

IPCC Climate Change 2014: Synthesis Report

Contribution of Working Groups I, II and III to the Fifth Assessment Report of the

Intergovernmental Panel on Climate Change [Core Writing Team, R.K. Pachauri and L.A. Meyer (eds.)]

IPCC, Geneva, Switzerland (2014)

151 pp

[Iyer et al., 2008](#)

K. Iyer, B. Jamtveit, J. Mathiesen, A. Malthe-Sørenssen, J. Feder **Reaction-assisted hierarchical fracturing during serpentinization**

Earth Planet. Sci. Lett., 267 (3–4) (2008), pp. 503-516

[ArticleDownload PDFView Record in Scopus](#)

[Johnson et al., 1](#)

J.W. Johnson, E.H. Oelkers, H.C. Helgeson **SUPCRT92: a software package for calculating the standard molal thermodynamic properties of minerals, gases, aqueous species, and reactions from 1 to 5000 bar and 0 to 1000 °C**

Comput. Geosci., 18 (7) (1992), pp. 899-947

[ArticleDownload](#) [PDFView](#) [Record in Scopus](#)

[Johnson et al., 2](#)

N.C. Johnson, B. Thomas, K. Maher, R.J. Rosenbauer, D. Bird, G.E. Brown **Olivine dissolution and carbonation under conditions relevant for in situ carbon storage**

Chem. Geol., 373 (2014), pp. 93-105

<http://doi.org/10.1016/j.chemgeo.2014.02.026>

[ArticleDownload](#) [PDFView](#) [Record in Scopus](#)

[Kelemen and Hir](#)

P.B. Kelemen, G. Hirth **Reaction-driven cracking during retrograde metamorphism: olivine hydration and carbonation**

Earth Planet. Sci. Lett., 345 (2012), pp. 81-89

[ArticleDownload](#) [PDFView](#) [Record in Scopus](#)

[Kelemen and Ma](#)

P.B. Kelemen, J. Matter **In situ carbonation of peridotite for CO₂ storage**

Proc. Natl. Acad. Sci. USA, 105 (45) (2008), pp. 17295-17300

[CrossRefView](#) [Record in Scopus](#)

[Kelemen et al., 2](#)

P.B. Kelemen, J. Matter, E.E. Streit, J.F. Rudge, W.B. Curry, J. Blusztajn **Rates and mechanisms of mineral carbonation in peridotite: natural processes and recipes for enhanced, in situ CO₂ capture and storage**

Annu. Rev. Earth Planet. Sci., 39 (2011), pp. 545-576

[CrossRefView](#) [Record in Scopus](#)

[King et al., 2010](#)

H.E. King, O. Plümper, A. Putnis **Effect of secondary phase formation on the carbonation of olivine**

Environ. Sci. Technol., 44 (16) (2010), pp. 6503-6509

[CrossRefView](#) [Record in Scopus](#)

[Kutchko et al., 20](#)

B.G. Kutchko, B.R. Strazisar, D.A. Dzombak, G.V. Lowry, N. Thaulow **Degradation of well cement by CO₂ under geologic sequestration conditions**

Environ. Sci. Technol., 41 (13) (2007), pp. 4787-4792

[CrossRefView](#) [Record in Scopus](#)

[Lackner et al., 19](#)

K.S. Lackner, C.H. Wendt, D.P. Butt, E.L. Joyce Jr, D.H. Sharp **Carbon dioxide disposal in carbonate minerals**

Energy, 20 (11) (1995), pp. 1153-1170

[ArticleDownload PDFView Record in Scopus](#)

[Lucier and Zoba](#)

A. Lucier, M. Zoback **Assessing the economic feasibility of regional deep saline aquifer CO₂ injection and storage: a geomechanics-based workflow applied to the Rose Run sandstone in Eastern Ohio, USA**

Int. J. Greenh. Gas Control, 2 (2) (2008), pp. 230-247

[ArticleDownload PDFView Record in Scopus](#)

[Luquot and Gouze](#)

L. Luquot, P. Gouze **Experimental determination of porosity and permeability changes induced by injection of CO₂ into carbonate rocks**

Chem. Geol., 265 (1) (2009), pp. 148-159

[ArticleDownload PDFView Record in Scopus](#)

[Mason et al., 2013](#)

H.E. Mason, W.L. Du Frane, S.D. Walsh, Z. Dai, S. Charnvanichborikarn, S.A. Carroll **Chemical and mechanical properties of wellbore cement altered by CO₂-rich brine using a multianalytical approach**

Environ. Sci. Technol., 47 (3) (2013), pp. 1745-1752

[CrossRefView Record in Scopus](#)

[Matter et al., 2016](#)

J.M. Matter, M. Stute, S.Ó. Snæbjörnsdóttir, E.H. Oelkers, S.R. Gislason, E.S. Aradóttir, W.S. Broecker **Rapid carbon mineralization for permanent disposal of anthropogenic carbon dioxide emissions**

Science, 352 (6291) (2016), pp. 1312-1314

[CrossRefView Record in Scopus](#)

[Meredith and Atkinson](#)

P.G. Meredith, B.K. Atkinson **Fracture toughness and subcritical crack growth during high-temperature tensile deformation of Westerly granite and Black gabbro**

Phys. Earth Planet. Inter., 39 (1) (1985), pp. 33-51

[ArticleDownload PDFView Record in Scopus](#)

[O'Connor et al., 2002](#)

W.K. O'Connor, D.C. Dahlin, G.E. Rush, C.L. Dahlin, W.K. Collins **Carbon dioxide sequestration by direct mineral carbonation: process mineralogy of feed and products**

Miner. Metallurgical Proc., 19 (2002)

(DOE/ARC-2002-006)

[O'Hanley, 1992](#)

D.S. O'Hanley **Solution to the volume problem in serpentinization**

Geology, 20 (8) (1992), pp. 705-708

[CrossRefView Record in Scopus](#)

[Olsson et al., 20](#)

J. Olsson, N. Bovet, E. Makovicky, K. Bechgaard, Z. Balogh, S.L.S. Stipp **Olivine reactivity with CO₂ and H₂O on a microscale: implications for carbon sequestration**

Geochim. Cosmochim. Acta, 77 (2012), pp. 86-97

<http://doi.org/10.1016/j.gca.2011.11.001>

[ArticleDownload PDFView Record in Scopus](#)

[Peuble et al., 20](#)

S. Peuble, M. Andreani, M. Godard, P. Gouze, F. Barou, B. Van De Moortele, B. Reynard **Carbonate mineralization in percolated olivine aggregates: linking effects of crystallographic orientation and fluid flow**

Am. Mineral., 100 (2008) (2015), pp. 474-482

[CrossRefView Record in Scopus](#)

[Peuble et al., 20](#)

S. Peuble, M. Godard, L. Luquot, M. Andreani, I. Martinez, P. Gouze **CO₂ geological storage in olivine rich basaltic aquifers: new insights from reactive-percolation experiments**

Appl. Geochem., 52 (2015), pp. 174-190

<http://doi.org/10.1016/j.apgeochem.2014.11.024>

[ArticleDownload PDFView Record in Scopus](#)

[Ragan, 1963](#)

D.M. Ragan **Emplacement of the Twin Sisters Dunite, Washington**

Am. J. Sci., 261 (1963), pp. 545-569

[Rutqvist, 2012](#)

J. Rutqvist **The geomechanics of CO₂ storage in deep sedimentary formations**

Geotech. Geolog. Eng., 30 (3) (2012), pp. 525-551

[CrossRefView Record in Scopus](#)

[Seifritz, 1990](#)

W. Seifritz **CO₂ disposal by means of silicates**

Nature, 345 (1990), p. 486

[CrossRefView Record in Scopus](#)

[van Noort et al.,](#)

R. van Noort, C.J. Spiers, M.R. Drury, M.T. Kadianis **Peridotite dissolution and carbonation rates at fracture surfaces under conditions relevant for in situ mineralization of CO₂**

Geochim. Cosmochim. Acta, 106 (2013), pp. 1-24

[ArticleDownload PDFView Record in Scopus](#)

[Vilarrasa and Ca](#)

V. Vilarrasa, J. Carrera **Geologic carbon storage is unlikely to trigger large earthquakes and reactivate faults through which CO₂ could leak**

Proc. Natl. Acad. Sci., 112 (19) (2015), pp. 5938-5943

[CrossRefView Record in Scopus](#)

[Walsh, 1965](#)

J.B. Walsh **The effect of cracks on the compressibility of rocks**

J. Geophys. Res., 70 (1965), pp. 381-389

[CrossRef](#)

[Wolterbeek et al., 2016](#)

T.K. Wolterbeek, S.J. Hangx, C.J. Spiers **Effect of CO₂-induced reactions on the mechanical behaviour of fractured wellbore cement**

Geomech. Energy Environ., 7 (2016), pp. 26-46

[ArticleDownload PDFView Record in Scopus](#)

[Xu et al., 2013](#)

Jie Xu, C. Yan, F. Zhang, H. Konishi, H. Xu, H. Teng **Testing the cation-hydration effect on the crystallization of Ca-Mg-CO₃ systems**

Proc. Natl. Acad. Sci., 110 (44) (2013), pp. 17750-17755

[CrossRefView Record in Scopus](#)

[Zhu et al., 2016](#)

W. Zhu, F. Fousseis, H. Lisabeth, T. Xing, X. Xiao, V. De Andrade, S.I. Karato **Experimental evidence of reaction-induced fracturing during olivine carbonation**

Geophys. Res. Lett., 43 (18) (2016), pp. 9535-9543

[CrossRefView Record in Scopus](#)

[Zoback and Byerlee, 1975](#)

M.D. Zoback, J.D. Byerlee **Permeability and effective stress: geologic notes**

Am. Assoc. Pet. Geol. Bull., 59 (1975), pp. 154-158

<http://doi.org/10.1306/83D91C40-16C7-11D7-8645000102C1865D>

[View Record in Scopus](#)

[Zoback and Zinke, 2002](#)

M.D. Zoback, J.C. Zinke **Production-induced normal faulting in the Valhall and Ekofish oil fields**

Pure Appl. Geophys., 159 (2002), pp. 403-420

[CrossRefView Record in Scopus](#)